

<sup>1</sup> Department of Atmospheric Science, Yunnan University, Kunming, P.R. China  
<sup>2</sup> Key Laboratory of Regional Climate-Environment Research for Temperate East Asia,  
Institute of Atmospheric Physics, Chinese Academy of Sciences, Beijing, P.R. China  
<sup>3</sup> Department of Atmospheric Science, Nanjing University, Nanjing, P.R. China

## Simulation of direct effects of black carbon aerosol on temperature and hydrological cycle in Asia by a Regional Climate Model

J. Wu<sup>1,2</sup>, C. Fu<sup>2</sup>, Y. Xu<sup>1</sup>, J. P. Tang<sup>3</sup>, W. Wang<sup>1</sup>, Z. Wang<sup>1</sup>

With 13 Figures

Received 18 October 2007; Accepted 20 January 2008  
Published online 14 August 2008 © Springer-Verlag 2008

### Summary

The simulation of direct radiative effect of black carbon (BC) aerosol over Asia is carried out with application of Regional Climate Model RegCM3 over the period of 1993–2003 based on BC emission inventory in 2000. Major findings are as follows. The column burden of BC exceeds  $1 \text{ mg/m}^2$  in central, eastern, and southern China with the highest value of  $2.5 \text{ mg/m}^2$  over Sichuan Basin of China, and is of  $1\text{--}2 \text{ mg/m}^2$  in India subcontinent. The column averaged advection field of BC shows an eastward tendency in north of  $20^\circ \text{ N}$ , whereas an opposite trend is found in south of  $10^\circ \text{ N}$ . Off-line radiative forcing (RF) induced by BC, which is due to direct absorption or scattering of BC, is positive at the top of the atmosphere (TOA), while maximum effect is found over Sichuan Basin. The RF is of  $1\text{--}1.5 \text{ W/m}^2$  in areas such as the middle and low reaches of the Yangtze River, East China Sea, South China Sea, Indo-China Peninsula and most parts of Indian subcontinent. Surface RF is found to be negative and its absolute value is larger than that at TOA. Based on simulation results, BC's impacts on temperature, stratification stability, water vapor, precipitation and evaporation etc., are primarily characterized by cold-and-wet change in southern and northwest China, cold-and-dry change in northern and northeast China, warm-and-wet change of

India subcontinent, as well as warm-and-dry change of Central Asia.

### Introduction

As BC's single scattering albedo is smaller than most kinds of aerosols, it absorbs more solar radiation, which in turn decreases solar radiation absorbed by the surface. By absorbing and emitting infrared radiation, BC also changes the infrared radiation characteristic of the atmosphere. Accordingly, BC can disturb the radiative balance of the earth-atmosphere system and then affect the climate change (Hansen et al. 1997; Hansen and Nazarenko 2004; Roberts and Jones 2004).

In recent years, BC's radiative effects have been studied extensively. The global annual averaged RF values of external mixture of  $0.20 \text{ W/m}^2$  and  $0.16 \text{ W/m}^2$  were obtained by Haywood et al. (1997) and Myhre et al. (1998) respectively, and the internal mixture of BC and sulfate would lead to stronger RF. Cooke et al. (1999) reported a global burden of BC of  $0.14 \text{ mg/m}^2$  and radiative forcing value of  $0.17 \text{ W/m}^2$ , while Jacobson (2000) obtained the RF of  $0.54 \text{ W/m}^2$  and

Correspondence: Jian Wu, Department of Atmospheric Science, Yunnan University, Kunming, P.R. China (E-mail: wujian@ynu.edu.cn)

normalized direct RF of 1200 W/g by numerical simulations. The estimate of the global averaged BC direct RF value was  $0.2 \pm 0.15 \text{ W/m}^2$  in the fourth assessment report of Intergovernmental Panel on Climate Change (IPCC) (Forster et al. 2007). Jacobson (2002) argued that BC aerosol would make the surface temperature increase 0.35 K in five years based on the original emission data (Cooke et al. 1999). Jacobson (2004) updated the surface temperature change caused by BC and organic carbon (OC) to 0.27 K based on the up-to-date emission data (Bond et al. 2004).

Menon et al. (2002) simulated direct effects of BC over China and India with general circulation model (GCM). They found that the BC over China, India, and Indian Ocean would cool the Chinese surface temperature of 0.5–1.0 K in summer but heat other areas. Their research showed that precipitation would increase notably in southern China and India but decrease in northern China. In addition, they pointed out that climate change caused by black carbon was not limited to areas with large black carbon distribution.

Recently, the Community Atmospheric Model (CAM) was applied to simulate BC's radiative effects (Wang 2004). One of their main findings was the change in hydrological cycle caused by BC, particularly the precipitation change in tropics, which was confirmed by Roberts and Jones (2004) and Chung and Seinfeld (2005). Wang (2004) also noticed that BC causes no distinct change in surface temperature (only slight rise of 0.09 K), but BC imposes more significant regional impacts on climate. The research of Chung and Seinfeld (2005) showed that under external mixture condition, BC and sulfate would rise global average surface temperature by 0.20 K (0.29 K in the Northern Hemisphere and 0.11 K in the Southern Hemisphere) and increase precipitation over 0–20° N while decreasing over 0–20° S. If under internal mixture condition at the same concentration, the rise of global average temperature would be 0.37 K (0.54 K in the Northern Hemisphere and 0.20 K in the Southern Hemisphere) with more significant precipitation change than the experiments with external mixture. The most remarkable temperature change occurred in high latitude area of the Northern Hemisphere in winter and spring with global average BC climate sensitivity being  $0.6 \text{ K/W m}^2$ . To investigate the climate sensibility to BC,

Roberts and Jones (2004) quadrupled BC emission to improve the signal to noise ratio in simulations. Their results of 30-year integration using atmosphere-ocean coupled model showed that there was linear correlation between value of global average RF and BC emission amount, and the climate sensitivity factor was  $0.56 \pm 0.06 \text{ K/W m}^2$ . Phenomena such as global heating and Intertropical Convergence Zone (ITCZ) northwards moving were found around the globe except in China, India, and a part of Africa. The above-mentioned literatures are carefully-designed modeling efforts in addressing the issue of climate effect of BC, though only direct effects are taken into consideration.

Researches show distinct regional radiative effects of BC (Ramanathan et al. 2001a, b, 2005; Wu et al. 2004). Ramanathan et al. (2005) claimed that Atmospheric Brown Cloud (ABC) with BC as one of the major ingredients could impact the climate change in India area in eight aspects. Considered both global warming and aerosol RF, their simulation results closely resemble the observations, indicating ABC's direct impact on Indian climate change, in particular the Indian monsoon.

Almost all current results of BC's radiative effects are obtained via simulations using of GCMs. Since long-term integration is required, most simulations employed only coarse grids, which may be improper to identify the regional characteristics of BC's radiative effects. Relevant literatures also show some uncertainties. Inconsistent results appear in different works despite some results of different researches are quite similar. More modeling efforts are needed to recognize these problems. To reveal distinct regional characteristics of BC's radiative effects, we simulate regional climate using a Regional Climate Model with fine resolution. Because Asia is one of the main aerosol source areas on the globe, more distinct radiative effects of BC should be observed in Asia. It is of our interests to study BC aerosol distribution characteristic, RF and climate response in Asia, and pay special attention to the relation between BC and precipitation.

The paper is organized as following. The model and simulation strategy is described in Sect. 1. Section 2 presents the control simulation results. Section 3 describes the climate effects of BC. Conclusions and discussions are given in Sect. 4.

## 1. Model and simulation strategy

### 1.1 Regional climate model description

In the current study, the Regional Climate Model version 3 (RegCM3, Giorgi et al. 2002) is used to simulate direct radiative effects of BC in Asia to investigate the possible climate change induced by BC, especially on temperature and hydrological cycle. Comparing to its precursor RegCM2, RegCM3 includes a new large-scale cloud and precipitation scheme considering subgrid-scale variabilities of clouds (Pal et al. 2000), the new parameterization schemes for ocean surface fluxes (Zeng et al. 1998) and a cumulus convection parameterization scheme (Betts 1986). Besides, a sulfate aerosol transport model, which solves a prognostic equation accounting for advection, turbulent diffusion and all kinds of deposition (Qian et al. 2001), is also integrated into the new version. RegCM3 uses the radiative transfer scheme of NCAR Community Climate Model version 3 (CCM3, Kiehl et al. 1996). The solar component of the radiative transfer scheme accounting for the effects of  $O_3$ ,  $H_2O$ ,  $CO_2$ , and  $O_2$ , follows the  $\delta$ -Eddington approximation of Kiehl et al. (1996), which includes 19 spectral intervals from 0.2 to 5  $\mu m$ . The cloud scattering and absorption parameterization follows Slingo (1989), whereby the optical properties of the cloud droplets (extinction optical depth, single scattering albedo, and asymmetry parameter) are expressed in terms of the cloud liquid water content and an effective droplet radius. When cumulus clouds are formed, the grid point fractional cloud cover is such that the total cover for the column extending from the model-computed cloud-base level to the cloud-top level (calculated assuming random overlap) is a function of horizontal grid point spacing. The thickness of the cloud layer is assumed to be equal to that of the model layer.

### 1.2 BC aerosol parameterization

Based on the sulfate transport model in RegCM3, a new transport model of BC is developed to calculate its distribution. BC is assumed to have a single log-normal size distribution with a standard deviation of 2.0 and a mode radius of 0.0118  $\mu m$  (d'Almeida et al. 1991). The mass-mixing ratio is the only prognostic variable to describe the atmospheric transport of BC aerosols. The bulk dry deposition speed, gravitational sedimentation speed, and wet scavenging processes of BC are the same as those chosen by Wang (2004). The emission rate of BC in 2001 is adopted (Streets et al. 2003), which excludes emission of Russia and this may underestimate BC concentration in Asia. Due to the difficulty of harmonizing different emission data, we used only emission data of Streets et al. (2003). The emission data includes annually averaged anthropogenic and biomass burning emission. The annually averaged emission used in this simulation is summarized in Table 1. It shows the annual total emission of the model domain can reach 2451.7 Gg/yr, in which the three investigated region occupies 15% for south of China, 18% for north of China, and 24% for India sub-continent respectively. Chinese emission takes the percentage of 41% in the model domain (Streets et al. 2003).

The effects of BC on radiation are simulated based on  $\delta$ -Eddington approximation in current CCM3 radiation scheme. The normalized radiative characteristics of BC for each waveband in CCM3 are adopted from d'Almeida et al. (1991). The optical parameters of BC aerosol for the waveband of 0.35–0.64  $\mu m$  are adopted from Haywood and Shine (1995), and the specific extinction coefficient is 12.50  $m^2/g$ , single scattering albedo is 0.25, and asymmetry factor is 0.42. BC's impact on infrared radiation is ignored in current study.

**Table 1.** Annual emission of BC used in this simulation for the investigated regions (Gg/yr)

	South of China (22–30° N, 100–120° E)	North of China (32–50° N, 105–120° E)	India sub-continent (10–28° N, 70–90° E)	Whole domain
Total emission (Gg/yr)	371.1	441.3	592.3	2451.7
Emission rate ( $10^{-9} g/m^2 \cdot s^{-1}$ )	5.39	3.71	4.44	0.95

### 1.3 Experiment design

The horizontal resolution of the model is 90 km with  $120 \times 90$  grid points. There are 14 sigma levels stretching from the surface up to 100 hPa. The sigma values of the lower five levels are 0.84, 0.86, 0.93, 0.96, 1.00, respectively. NCAR/NCEP reanalysis data is used to provide initial conditions and boundary values every 6 hr. Exponent relaxation scheme is chosen to deal with lateral boundaries. The model atmosphere is forced by 1-degree resolution NOAA Optimum Interpolation Sea Surface Temperature (OISST) data. The model is integrated from 1st February 1993 to 1st March 2003. The first month is regarded as spin-up time, while only averaged results of the last 10 years are analyzed. Other schemes include Grell convective parameterization (Grell 1993), and Holtslag et al. (1990) PBL parameterization.

Two experiments are conducted using the same parameters except one with BC, which simulates BC direct radiation effect (BDR), and the other without BC, which is control experiment (CON). The results from these two experiments are compared, particularly the direct radiative forcing of BC. The direct radiative forcing of BC is estimated by the difference of net downward radiative flux at top of the model between these two runs. The indirect radiative effects are not included in this study.

## 2. Control experiment

### 2.1 Climate simulation

In this section, we discuss simulation results of the control run to evaluate the basic climatic

simulation. Figure 1 shows 10 year mean temperature on 850 hPa of NCEP reanalysis data (Fig. 1a) and simulation results (Fig. 1b), and the contour in Fig. 1b shows their statistically significant correlation coefficient. The simulated results agree well with reanalysis data in most part of model domain. The temperature patterns over most part of lower latitude region are well captured, and the correlation coefficient can reach 0.9 in the north of  $20^\circ$  N. However, the simulation is  $2\text{--}3^\circ\text{C}$  cooler than NCEP data in eastern China, and  $2\text{--}3^\circ\text{C}$  warmer than NCEP data at eastern boundary region. We also compared simulated temperature on other levels (not shown). The temperature patterns are also well captured by the model, and the cool bias on 850 hPa reduces on higher levels.

The grid rainfall data of Global Precipitation Climatology Project (GPCP) is used to compare with simulation result (Adler et al. 2003). Figure 2 shows annual mean and summer precipitation in GPCP data (Fig. 2a and c) and simulation (Fig. 2b and d) respectively. In observation data, the rainfall shows two narrow bands with one northeast-southeast orientation the other west-east orientation for annual mean and summer. The northeast-southeast orientation band covers most part of northeast China, Korea Peninsular, and part of Japan with its maximum of 7 mm/dy. Simulation underpredicts its maximum over northeast and northern China in annual mean, but captures its pattern over Japan. There exists a west-east orientation rainfall band in observation data both in annual mean and in summer with maximum of 9 mm/dy and 12 mm/dy respectively. This band is well cap-

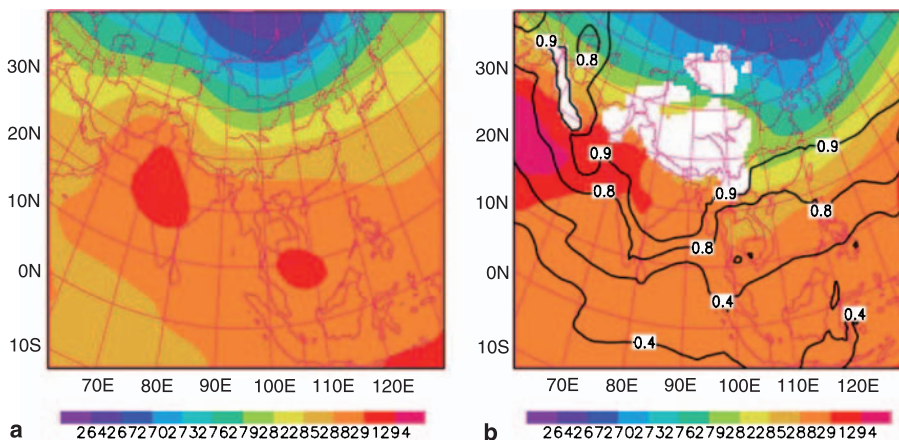


**Fig. 1.** Temperature on 850 hPa of NCEP data (a) and simulated of CON experiment (b), units K. Contour indicates statistically significant correlation coefficient

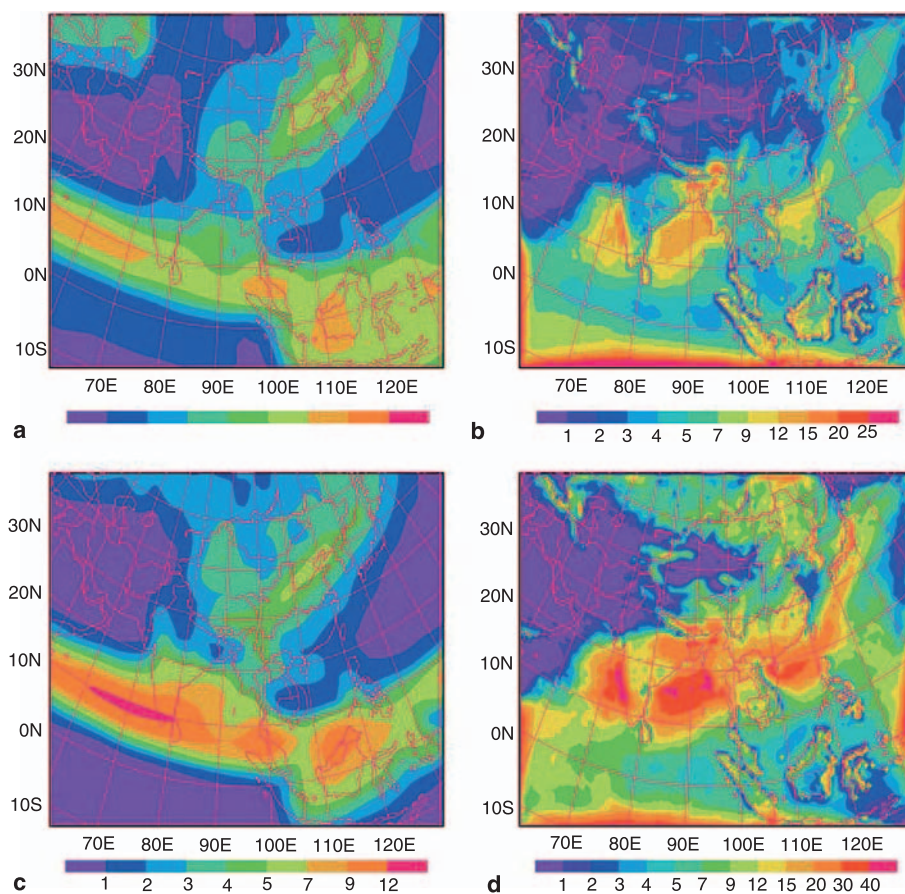


**Fig. 2.** Observation and simulated precipitation in annual mean and summer (mm/dy). (a) Observation of annual mean, (b) simulation in annual mean, (c) observation in summer, and (d) simulation in summer

tured in simulation especially between 60 and 100° E, though simulation underpredicts precipitation over southeast region of the model domain for 3–4 mm/dy. Figure 2d shows that the structure of Meiyu rain band associated with the East Asian summer monsoon is captured, though simulation results are bigger than observation, which

should relate to their different resolution for simulation and observation data.

## 2.2 BC simulation

The concentration and column burden of BC are shown in Fig. 3. The column burden of BC ex-

**Table 2.** Results comparison of ours and other simulations

Model	Column burden of BC ( $\text{mg}/\text{m}^2$ )	RF at TOA ( $\text{W}/\text{m}^2$ )	Normalized RF at TOA ( $\text{W}/\text{g}$ )	References
SPRINT	–	0.36	–	Takemura et al. (2001)
LOA	0.37	0.55	1486	Reddy et al. (2005)
GISS	0.29	0.61	2103	Hansen et al. (2005)
GISS	0.29	0.35	1207	Koch (2001)
GISS	0.39	0.50	1282	Chung and Seinfeld (2002)
GISS	0.43	0.53	1233	Liao and Seinfeld (2005)
SPRINTARS	0.53	0.42	792	Takemura et al. (2005)
GATORG	0.39	0.55	1410	Jacobson (2001)
CCM	0.33	0.34	1030	Wang (2004)
UIO-GCM	0.30	0.19	633	Kirkevåg and Iversen (2002)
RegCM3 Whole domain	0.45	0.32	711	Current simulation
RegCM3 North of China	0.55	0.64	1164	Current simulation
RegCM3 South of China	1.42	1.55	1092	Current simulation
RegCM3 India sub-continent	1.22	1.36	1115	Current simulation

ceeds  $1 \text{ mg/m}^2$  in central, eastern, and southern China, and amounts to  $2 \text{ mg/m}^2$  in some areas in northern and eastern China. A value of  $1\text{--}2 \text{ mg/m}^2$  is found in India subcontinent. The maximum value in the model domain is  $2.5 \text{ mg/m}^2$  located in Sichuan Basin of China, which is due to complex terrain in this basin. Column burden of BC from this simulation and GCMs are summarized in Table 2. Results from GCMs refer to average of whole globe, and BC burden over different part of model domain in this simulation are bigger than the global average, especially in South of China and India, where it can reach  $1.42$  and  $1.22 \text{ mg/m}^2$  respectively. Global averaged burden from different GCMs simulations is  $0.38 \text{ mg/m}^2$ , but it is  $0.45 \text{ mg/m}^2$  over the whole domain of this simulation, which infers more distinct radiative forcing over Asian domain.

The characteristic of the surface concentration distribution is similar to that of column burden, with a maximum value of  $3 \mu\text{g/m}^3$  in Sichuan

Basin, and over  $2 \mu\text{g/m}^3$  in central and southern China. The surface concentration is  $1.5\text{--}2.5 \mu\text{g/m}^3$  in India subcontinent. In Indo-China Peninsula, it is  $1.5\text{--}2 \mu\text{g/m}^3$ . It reads between  $0.3\text{--}0.8 \mu\text{g/m}^3$  in Malaysia, Indonesia, and Philippine. Comparison of BC's surface concentration in this simulation with observation data is listed in Table 3, which reveals big error in cities of China. In fact, it is difficult to capture concentration of BC in cities with coarse grid cells and emission data. Simulation gives much better agreement with observation data from Asian Pacific Regional Aerosol Characterization Experiment (ACE-Asia), though simulation is somewhat lower at part of these observatories located in the northeast of model domain, which may relate to lack of Russian emission data in this work. In addition, the pattern of surface concentration in our simulation is consistent with concentration  $75 \text{ m}$  above the surface simulated by Zhang et al. (2005).

As panel (a) of Fig. 3 shows, column averaged advection streamline demonstrates the basic west-

**Table 3.** Comparison of BC's surface concentration with observation data

Position	Time	Observation ( $\mu\text{g/m}^3$ )	Simulation ( $\mu\text{g/m}^3$ )	References
Beijing ( $39.90^\circ \text{ N}$ , $116.30^\circ \text{ E}$ )	2002.07–08	5.40	0.63	He et al. (2004)
Shanghai ( $31.2^\circ \text{ N}$ , $121.4^\circ \text{ E}$ )	Annual average of 1999	6.50	0.46	Ye et al. (2003)
Guangzhou ( $23.1^\circ \text{ N}$ , $113.2^\circ \text{ E}$ )	2001.01–02	8.30	0.80	Cao et al. (2003)
Kwangju ( $35.15^\circ \text{ N}$ , $126.91^\circ \text{ E}$ )	2002.07–08	0.30	0.23	Cao et al. (2003)
Rishiri-tō ( $45.12^\circ \text{ N}$ , $141.20^\circ \text{ E}$ )	2001.03–04	0.40	0.21	He et al. (2004)
Sado-shima ( $38.25^\circ \text{ N}$ , $138.40^\circ \text{ E}$ )	2001.03–04	0.63	0.41	Uno et al. (2004)
Hachijō-jima ( $33.15^\circ \text{ N}$ , $139.75^\circ \text{ E}$ )	2001.03–04	0.33	0.29	Uno et al. (2004)
Amamiō-shima ( $28.44^\circ \text{ N}$ , $129.70^\circ \text{ E}$ )	2001.04	0.63	0.42	Uno et al. (2004)
Chichi-jima ( $27.07^\circ \text{ N}$ , $142.22^\circ \text{ E}$ )	Annual average of 2001	0.21	0.19	Uno et al. (2004)
Oki-shotō ( $36.20^\circ \text{ N}$ , $133.20^\circ \text{ E}$ )	2001.03–04	0.52	0.40	Uno et al. (2004)
Tokara-rettō ( $29.5^\circ \text{ N}$ , $128^\circ \text{ E}$ )	2001.04–05	0.36	0.22	Uno et al. (2004)

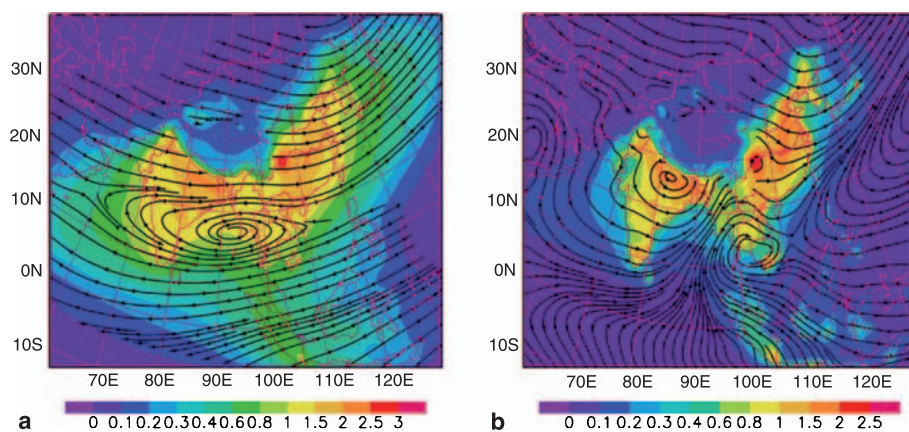


**Fig. 3.** Column burden of BC ( $\text{mg/m}^2$ ) and surface concentration ( $\mu\text{g/m}^3$ ). (a) Column burden and column average advection streamline and (b) surface concentration and layer-averaged advection streamline between  $700$  and  $850 \text{ hPa}$

to-east tendency to the north of  $20^{\circ}$  N, whereas an opposite trend is found to the south of  $10^{\circ}$  N. Strong anticyclonic advection is observed over Bay of Bengal, where the airflow in the west and north sides can advect BC over India subcontinent and Indo-China Peninsula into southern China. In panel (b) the low level advection shows that there is cyclonic advection over India, but still anticyclonic over Indo-China Peninsula. Besides, due to advection of southwest airflow over Bay of Bengal, BC from north Indian Ocean can affect Bengal and its adjacent regions. BCs over northern China can be advected into Korea Peninsula and Japan by the northwest airflow, meanwhile that over southern China can be transported to southern and eastern offing to Japan by the southwest airflow. BC from Indonesia and Malaysia will affect Indo-China Peninsula and Bay of Bengal by the southeast airflow.

### 3 Climate effects of BC

#### 3.1 Radiative forcing

In Fig. 4, RF at TOA and surface (SRF) are shown, the shading and contour stand for RF at TOA and SRF respectively. RF at TOA is positive, and it is bigger in the middle reach of the Yangtze River and northern India than other

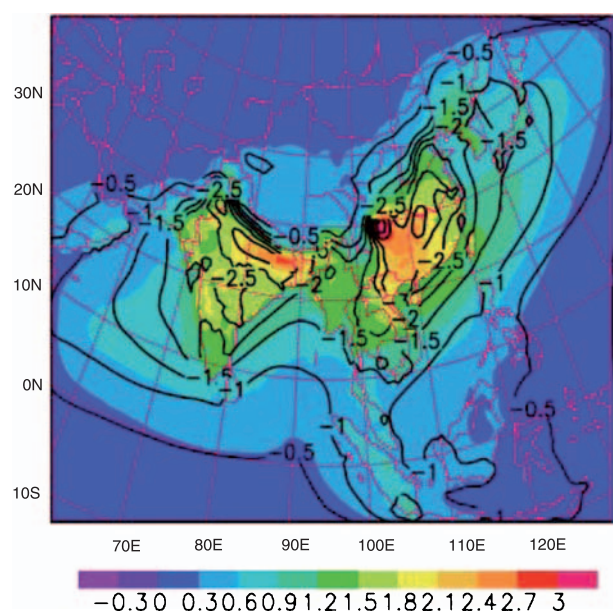


**Fig. 4.** Radiative forcing ( $\text{W}/\text{m}^2$ ) (shading: radiative forcing at TOA; contour: radiative forcing on surface)

areas. It can reach  $2.5 \text{ W}/\text{m}^2$  over Sichuan Basin, and is between  $1.5$  and  $2 \text{ W}/\text{m}^2$  in northern India. RF is within  $1$ – $1.5 \text{ W}/\text{m}^2$  in the middle and down stream areas of Yangtze River, East China Sea, South China Sea, Indo-China Peninsula, and India subcontinent. RF at TOA over the whole model domain, north of China, south of China, and India are listed in Table 2. RF of GCMs is also given. The average RF of GCMs is  $0.44 \text{ W}/\text{m}^2$ . It is  $0.32 \text{ W}/\text{m}^2$  in this simulation. Bigger averaged values of three investigated domains give proof to the heterogeneity of BC and RF over Asia, but their normalized RF agrees with GCMs.

The surface RF is negative, and its main distribution characteristic is similar to that of RF at TOA, but the absolute value is larger. It indicates that BC decreases surface incoming radiation. The most notable value appeared in Sichuan Basin, which agrees well with RF at TOA and BC burden. In Table 4, RF at SRF is more distinct than that at TOA (shown in Table 2), which may decrease surface temperature and evaporation. The main reason accounting for negative surface RF is that BC increases the absorption of solar radiation of atmosphere, and affects cloud cover.

#### 3.2 Temperature change

Due to radiative change, BC results in temperature variations. Figure 5 shows the change of daily mean temperature (Fig. 5a) and diurnal range (Fig. 5b) induced by BC. A two-tailed  $t$  test is conducted to indicate statistically significant areas in the Fig. 5 at the 90% confidence level according to Chervin and Schneider (1976). The surface temperature decrease is less than  $-0.2 \text{ K}$  in eastern and southern China at the presence of larger BC column burden. Temperature decreases are also found in northwest India and Pakistan, with the maximum of  $-0.4 \text{ K}$  found in the littoral to Indian Ocean. Though RF at SRF is almost negative in Fig. 4, heating belt also can be found in northeast and northern China, middle India, northern Kazakhstan and its adjacent areas. This simulation confirms that temperature change caused by black carbon is not limited to areas with large black carbon distribution, which is revealed by Menon et al. (2002).

Changes in the daytime highest and the daytime lowest temperature have also been investi-

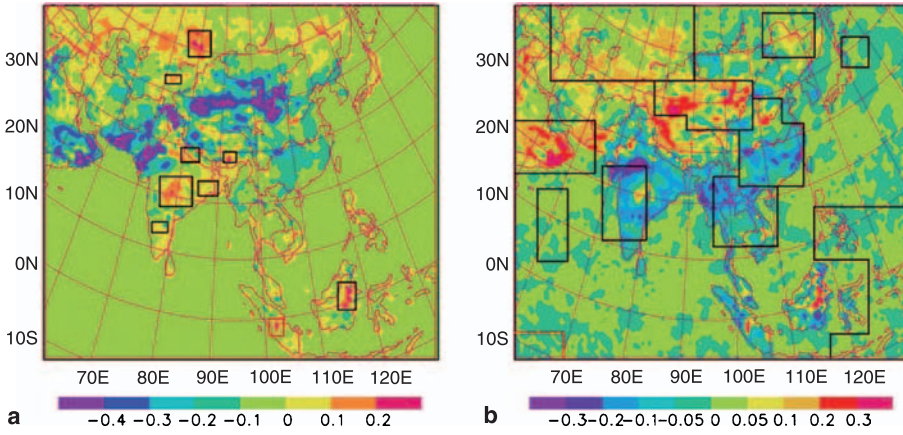


**Fig. 5.** Surface temperature change (K). Rectangle indicates areas in which the difference is statistically significant at the 90% confidence level according to a two-tailed *t*-test. (a) Daily mean temperature and (b) diurnal range

gated (figures not shown). In the Yellow River and Huai River plain, temperature decrease does not surpass  $-0.1$  K, and the same result can be found in northwest China. The maximum temperature drop (surpassing  $-0.1$  K) is observed in the north of Indo-China Peninsula. But in the middle of India, the rise of maximum temperature is also quite distinct, amounting to  $0.2$  K in some areas. The lowest temperature decreases slightly in China, particularly in the northwest area coinciding with the area of decreased daily average temperature. In most areas of India, the lowest temperature rises slightly.

The above-mentioned variation characteristics of daytime highest temperature and lowest temperature result in a reduction of surface temperature diurnal range in Indian subcontinent, Indo-China Peninsula and south of China shown in Fig. 5. The biggest drop of diurnal range ( $-0.3$  K) is found in northwest of India, while it rises  $0.1$ – $0.3$  K in northwest China, Central Asia and the Arabian Peninsula. Table 4 summarizes the change of annual mean temperature

and daily range of temperature for the investigated regions, which decreases in south of China and India and rises in north of China.

In order to understand the change of air temperature, its mass-weighted column averaged temperature change is showed in Fig. 6. In China,

**Table 4.** Annual mean RF at surface ( $RF_{srf}$ ,  $W/m^2$ ), change of surface temperature ( $T$ , K), daily range of temperature ( $T_r$ , K), temperature under  $700$  hPa ( $T_{low}$ , K) and above  $700$  hPa ( $T_{up}$ , K), precipitation ( $P_r$ , mm/dy), annual ( $V_{yr}$ , %) and summer mean ( $V_{su}$ , %) percent change of column vapor

	South of China	North of China	India sub-continent
$RF_{srf}$	-3.10	-1.69	-2.56
$T$	-0.08	-0.03	-0.06
$T_r$	-0.05	0.02	-0.05
$T_{low}$	-0.03	-0.03	0.02
$T_{up}$	0.03	0	0.04
$V_{yr}$	0.91	-0.52	0.15
$V_{su}$	2.01	-0.69	0.05
$P_r$	0.13	-0.10	-0.04

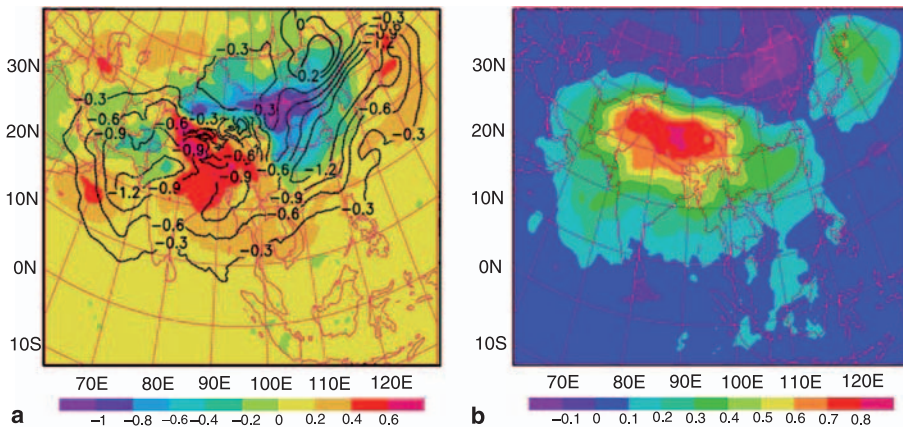


**Fig. 6.** Atmosphere temperature change ( $0.1$  K, shading). (a) Temperature change under  $700$  hPa (shading) and geopotential height change (gpm, contour), (b) temperature change above  $700$  hPa

the temperature in the lower atmosphere decreases except Qinghai-Tibet Plateau. The temperature decrease is more distinct in the north region than in the south. The maximum decrease of  $-0.1$  K is found in the middle reach of Yellow River and Sino-Mongolian frontier. The value of surface temperature drop (see Fig. 5a) is bigger than that of lower atmosphere in Chinese mainland. As a result, the stability of the lower atmosphere over China increases. The extent of temperature drop in lower atmosphere in eastern India is larger than surface temperature drop, so that the lower atmosphere becomes less stable. There is a weak temperature rising belt ( $0.02$ – $0.04$  K) in the lower atmosphere extending from Bay of Bengal, Indo-China Peninsula and South China Sea, to Pacific ocean south and east to Japan. Because the sea surface temperature is prescribed by OISST data in the current simulation, the stability of lower atmosphere of this belt shows strengthening tendency in these areas. As shown in Fig. 6b, the temperature change in the upper atmosphere (above 700 hPa) is different from the lower atmosphere shown in Fig. 6a. In the upper atmosphere, the magnitude of the temperature change is one order smaller than the lower level. The temperature-rising areas lie primarily in the northeast China and part of northwest China. Temperature decrease is found in the rest areas.

By comparing Fig. 6(a) with (b), conclusion can be reached that the static stability of the upper level atmosphere increases in Mongolia, north of China as the temperature decreases more in the lower layer than in the upper layer. Because the temperature decreases in the lower layer and increases in the upper layer, the stability over the south of China also increases. Static stability of lower layer in India also increases. These feature can also be summarized from Table 4.

The regional averaged temperature profile is given in Fig. 7. The near ground temperature drop over northern and southern China is greater than its column averaged value, and in general it can stabilize the atmosphere stratification. The biggest temperature drop is in the boundary layer, which decreases the stratification stability inside the boundary level but increases above the boundary layer. There is a weak temperature rising tendency over India, with the maximum rise occurred near 700 hPa, which increases the stability under 700 hPa.

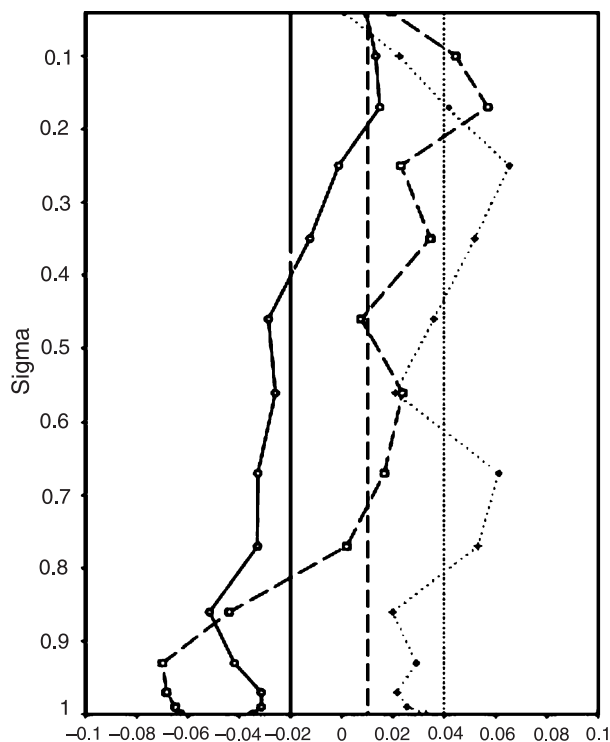
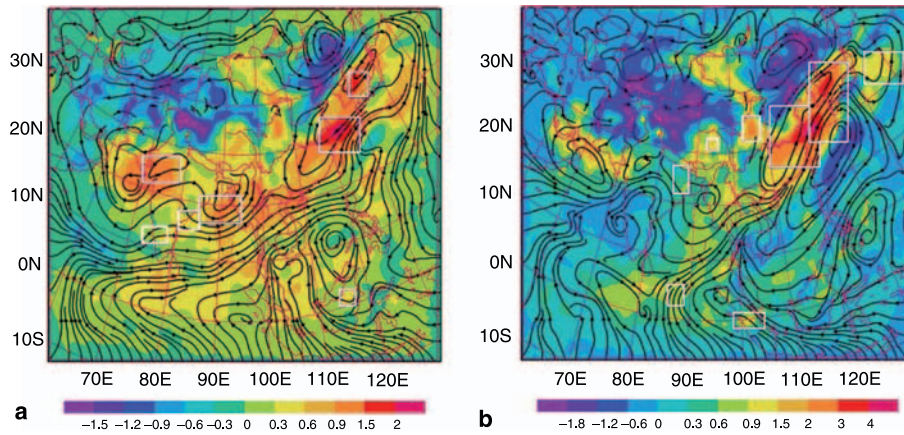


Fig. 7. Profile of temperature change and its vertical mean value (K, solid line: north of China; dashed line: south of China; and dotted line: India)

### 3.3 Effects on hydrological cycle

The changes of annual mean column vapor burden in percentage and the water vapor flux field below 700 hPa are shown in Fig. 8a. There exists a wide range belt with increased water vapor extending from western India, passing Bay of Bengal, Indo-China Peninsula, southern China, East China Sea, Korea Peninsula to regions nearby Japan, and the increasing rate of water vapor is above 0.6%. The maximum increasing rate of 2% appears over East China Sea near Shanghai. Another increased water vapor belt is found in areas extending from the west of Mongolia to Yellow River bend plain with a range between 0.3 and 0.9%. In northeast, northern, and northwest China and Central Asia, the water vapor burden is reduced by more than  $-0.3\%$ . Due to the effect of BC aerosol, the water vapor over eastern China shows a tendency of increasing in south but decreasing in north. While in northwest China and Central Asia, the vapor content reduces even further, which in turn induces greater effects on local environment and climate. This result is similar to the results of Ma et al. (2004).



**Fig. 8.** Annual mean and summer percent change of vapor column burden (%) and vapor flux change below 700 hPa. Rectangle indicates areas in which the difference is statistically significant at the 90% confidence level according to a two-tailed *t*-test. (a) Annual mean, and (b) summer

In their work, the tendency of increasing drought is revealed in northern and northeast China in recent years (Ma et al. 2004), and the trend is more notable in summer and autumn (Ma and Fu 2001).

In Fig. 8b, the wide-range excessive water vapor belt shown in panel (a) also appears in panel (b). In summer, the water vapor increase is most distinct in the belt from south of China, extending to East China Sea, Yellow Sea, Korea Peninsula until northeast–southwest Japan Sea. The increasing rate in summer in the belt is larger than its annually averaged value, especially in regions near Shanghai. In summer, the vapor content decreasing areas mainly lie in north of China, western China and Central Asia with a decreasing rate over  $-0.6\%$ .

The belt of increased vapor is resulted from the strengthened airflow, which is originated in Indian Ocean and South China Sea extending from southwest to northeast in the model domain. The streamlines from the south of China to the offing near Japan form a large scale cyclonic circulation, indicating a net water vapor convergence over this region. A similar cyclonic circulation can be found in western India and Bay of Bengal, which is in coincidence with the increased vapor content center. In north of China, a closed anticyclonic circulation region leads to net divergence in water vapor and decreased column burden. It is also noted that differential vapor can be transported from the north of Yangtze River to the south in eastern China,

weakening the vapor transport belt from the south of China to the north, thus reducing the water vapor in north of China. Table 4 shows vapor increase over south of China and India sub-continent of 0.91% and 0.15% for annual mean, and it is more distinct in summer. The decrease of vapor can also be found over north of China both in annual mean and summer mean. This pattern induces dry tendency in north of China and wet tendency in south of China.

The change in 700–850 hPa layer mean geopotential height field is plotted in Fig. 6a. A wide-range geopotential height decreasing belt is shown from the neighborhood near Arabian Peninsula to the east, passing India, Bay of Bengal, Indo-China Peninsula, South China Sea and East China Sea to Japan. This belt conforms to the vapor increase belt shown in Fig. 8a, and also complies with the zone where differential vapor advection is cyclonic. Evidently, due to the heating effect of BC in the lower atmosphere, the air pressure over these areas shows a declined tendency. Thus, the ambient water vapor is convergent in this area. It is also found that in north of China, the geopotential height increases slightly, consistent to the anticyclonic circulation of the differential vapor transport field in these areas. The increase of geopotential height and the divergence of water vapor in north of China are primarily caused by the temperature decrease in the lower atmosphere.

Annually averaged variation of column vapor burden in percentage from 1993 to 2002 calcu-

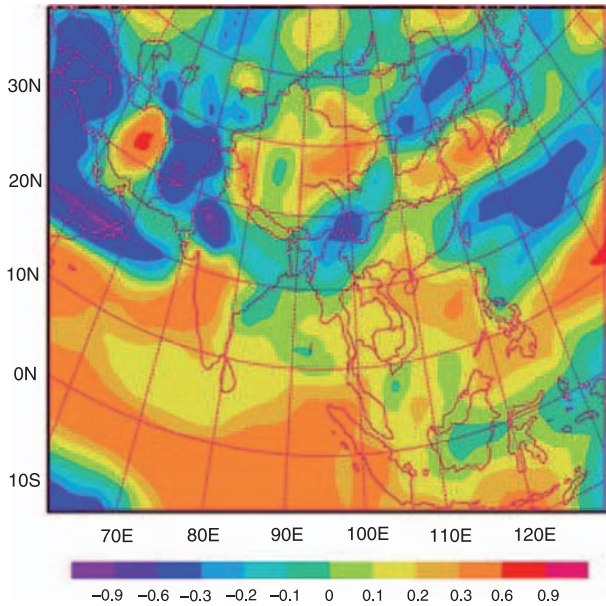


**Fig. 9.** Annual percentage change of column vapor burden from 1993 to 2002 in NCEP data

lated using NCEP data is illustrated in shading in Fig. 9. Vapor increasing is found in south of China with variation of 0.1–0.3%. It decrease in north of China by  $-0.2$  to  $-0.6\%$ . The pattern computed from NCEP data generally agrees well with the simulation throughout most of model domain. The simulation is, however, almost positive over East China Sea, where it is negative in NCEP data, and there also exists opposite pattern over Xinjiang. In addition, NCEP data gives smaller values than the simulation over south of China, Indo-China Peninsula, and most part of Indian sub-continent. Two possible reasons are: NCEP data includes more effects of green house gases, aerosols, and land cover change, etc. than what are considered in the current simulation; the SST can not be change by BC's RF in the current simulation.

To further analyze the water vapor transport, the latitudinal cross-section of vapor advection change averaged over  $32\text{--}35^\circ\text{N}$  is given in Fig. 10. In areas to the west of  $125^\circ\text{E}$ , negative vapor flux is found below 400 hPa. It infers the weakening of northward vapor flux. The largest value of  $-1\text{ g/kg}\cdot\text{m/s}$  appears in the boundary layer near  $115^\circ\text{E}$ . Obviously, the increase of southward vapor transport can lead to the decrease of water vapor column burden in north of China. On the contrary, the vapor transport

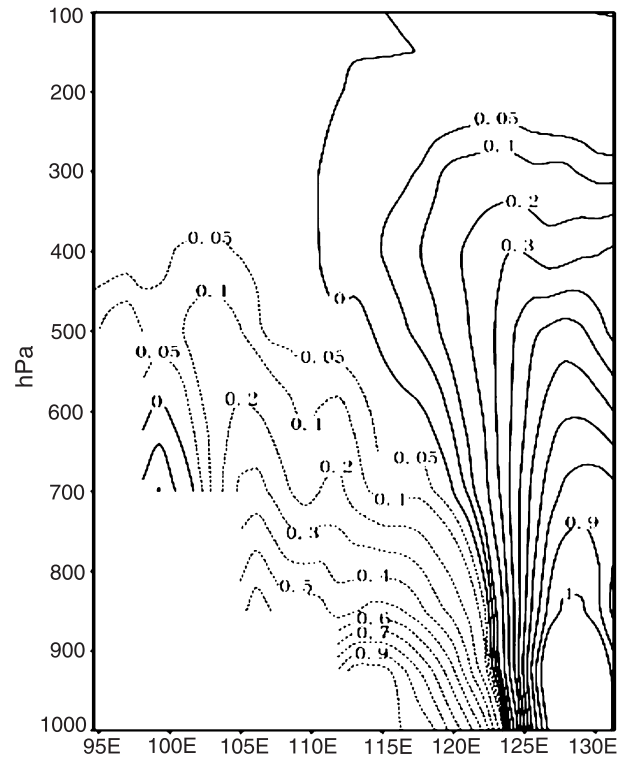


**Fig. 10.** Latitudinal cross section of vapor advection change averaged over  $32\text{--}35^\circ\text{N}$  (unit:  $\text{g/kg}\cdot\text{m/s}$ )

flux increment is positive to the east of  $125^\circ\text{E}$ . It indicates that BC leads to increase of northward vapor transport in this area. The largest value is  $1\text{ g/kg}\cdot\text{m/s}$  in the boundary layer over  $125\text{--}130^\circ\text{E}$ . The belt of increased vapor transport extends greatly in the vertical direction, and the increment can be as large as  $0.05\text{ g/kg}\cdot\text{m/s}$  even near 300 hPa. The enhanced northward vapor transport can increase water vapor in areas from south of China to northeast China and Japan vicinity.

The change of column vapor burden can affect precipitation. Annual mean changes of precipitation and surface evaporation are given in Fig. 11a and b. The annual mean precipitation increases in the center of Arabian Sea, Bay of Bengal, south of China, East China Sea, Korea Peninsula and east offing to Japan. While in the center of India subcontinent, Indo-China Peninsula, north of China, precipitation decreases with a maximum of  $-0.3$  to  $-0.4\text{ mm/day}$  in center India. Compared with Fig. 8, we find that both the surface and atmosphere show moistening tendency in Arabian Sea, Bay of Bengal, south of China, East China Sea and the offing to Japan. In Fig. 11b, the sur-

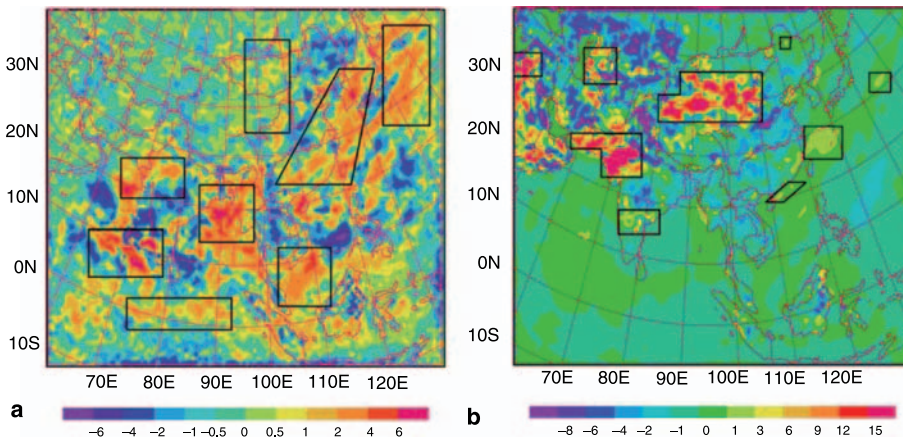


**Fig. 11.** Precipitation rate change and percent change of surface evaporation capacity. Rectangle indicates areas in which the difference is statistically significant at the 90% confidence level according to a two-tailed *t*-test. (a) Precipitation rate change (0.1 mm/dy) and (b) percent change of surface evaporation capacity (%)

face evaporation over areas of northwest India sub-continent and northwest China increases about 12–15% but generally decreases –4 to –8% in Central Asia. In most areas of India, north of China as well as Indo-China Peninsula, it decreases 1–2%. Table 4 shows precipitation over south of China can increase 0.13 mm/dy,

but it decreases over north of China and India sub-continent. The change of precipitation agrees well with the changes in column vapor in these regions except India sub-continent.

Based on the water vapor advection field shown in Fig. 8a, the increase of vapor column burden over south of China originates from the strengthening of northerly airflow from South China Sea. Hence, the enhanced evaporation over South China Sea, which is shown in Fig. 11b,

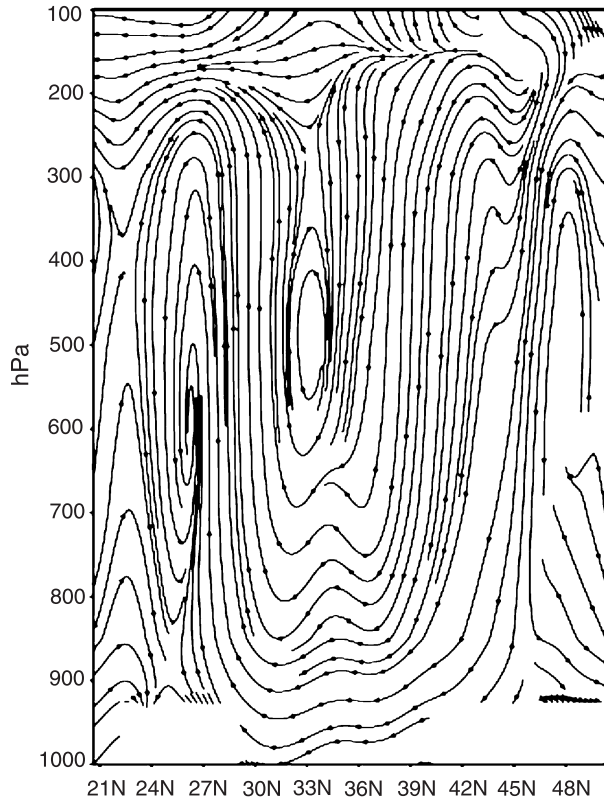


**Fig. 12.** Difference stream line along longitudinal section of 110–120° E

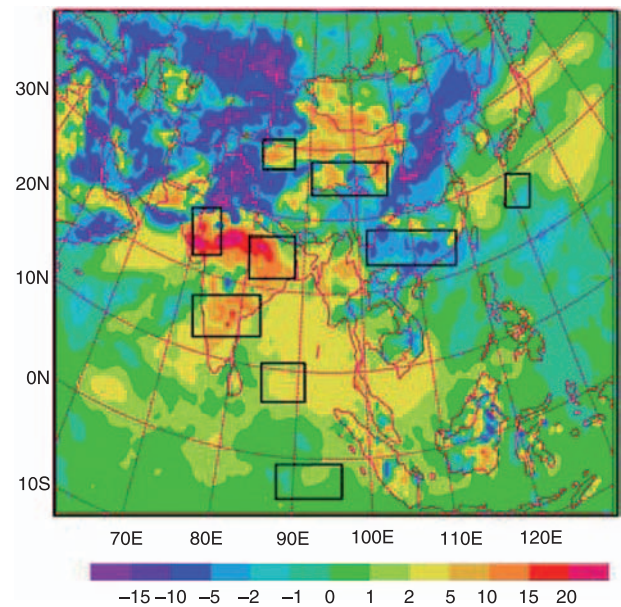


**Fig. 13.** Change of surface air specific humidity on 2 m height (0.01 g/kg). Rectangle indicates areas in which the difference is statistically significant at the 90% confidence level according to a two-tailed *t*-test

contributes largely to the increased vapor content in south of China.

In addition to the 0.6–1.5% increase of vapor in Fig. 8 over south of China, the 1–4% increase of precipitation in Fig. 11 over this area is also due to the possible change of vertical motion induced by BC. Figure 12 shows a longitudinal and vertical cross-section of the differential streamlines averaged over 110–120° E. BC makes the updraft strengthen remarkably between 24 and 30° N, which is consistent to precipitation-increasing area in the south of China. The subsidence is strengthened between 32 and 45° N in line with precipitation-decreasing area in north of China. Thereby precipitation increase in south of China is the result of increased vapor evaporation in South China Sea, increased water vapor transport to south of China as well as strengthened updraft in that area. In north of China, the suppressed precipitation is resulted from the reduced vapor and enhanced subsidence.

The change in specific humidity at 2 m above surface as illustrated in Fig. 13, can be caused by the changes in precipitation and evaporation. The surface air specific humidity increase is notably found in the north of Arabian Sea, India subcontinent, Bay of Bengal, Indo-China Peninsula, northwest China, middle and northern Pacific, and the increasing value can exceed 0.02 g/kg with a maximum of 0.2 g/kg in northwest India sub-continent. In northwest China, the specific humidity increase is a result of weak precipitation increase and distinct surface evaporation increase shown in Fig. 11. In Bay of Bengal, the increment is about 0.05 g/kg caused by the increase of offing evaporation in that area shown in Fig. 11b. In Central Asia, north of China, decrease of surface specific humidity can be found with the maximum of  $-0.1$  g/kg in downstream of Yellow River and Kazakhstan, which agrees well with the decrease of surface evaporation.

#### 4. Conclusion and discussion

We have performed regional simulations of climate, BC's direct radiative forcing and regional climatic effects of BC over Asian region. By comparing different runs, we discuss the change of temperature, air stability, water vapor content, precipitation and evaporation to indicate effects to temperature and hydrological cycle

over Asia. The main results of the current simulation of are:

- (1) The maximum of BC column burden is  $2.5 \text{ mg/m}^2$  in Sichuan Basin, which surpasses  $1 \text{ mg/m}^2$  in central, eastern and southern China, and  $1\text{--}2 \text{ mg/m}^2$  over India subcontinent. The basic tendency of column averaged transport streamline of BC is from west to east to the north of 20° N, whereas an opposite trend is found to the south of 10° N.
- (2) Radiative forcing induced by BC is big over the middle reach of the Yangtze River and northern India, with the maximum found in Sichuan Basin. It is  $1\text{--}1.5 \text{ W/m}^2$  in middle and downstream of the Yangtze River, East China Sea and South China Sea, Indo-China Peninsula and most areas of India subcontinent.
- (3) The surface temperature in most areas of China decreases up to  $-0.4 \text{ K}$ , with the maximum in northwest China. In south of China, the atmosphere is stabilized by cooling the lower layer while warming above.
- (4) Water vapor increases over 0.6% in the south of China but decreases over  $-0.3\%$  in the north. The increased vapor content in south of China is mainly caused by strengthening of the southerly airflow from South China Sea. The precipitation can be increased by  $0.4\text{--}0.6 \text{ mm/day}$  in south of China, but decreased in north of China. The change of vertical motion is also related to the change of precipitation.
- (5) Some tendencies of climate change on surface and lower atmosphere have been observed. More specifically, northwest and south of China tends to be cold and wet, north of China to be cold and dry, India sub-continent to be warm and wet, and Central Asia to be warm and dry. These tendencies can be well explained by above mentioned mechanism of how BC affecting temperature, stratification, water vapor, precipitation, evaporation and so on.

Some of limitation should be taken into account in evaluating our results. The primary one is that indirect effect of BC is not accounted for. A second source of uncertainty is that BC's effect on SST is not included in current study. Yet it is found that, BC can affect Indian Ocean SST

gradient, and further affecting Indian Monsoon (Ramanathan et al. 2005). Therefore the interaction between SST and BC as well as effects of SST on temperature and hydrological cycle should be considered with coupled climate and ocean model systems in the future. Third, no interannual and seasonal variation is considered in our experiments, which may induce uncertainty into BC concentration and its climatic effects. Fourth, we only consider BC in current work instead of internal or external mix with other kind of aerosol, which can change its radiative characters and may induce different climatic effects. Actually, BC seldom exists alone, so our simulations should be regarded as ideal experiments.

### Acknowledgment

The study are sponsored by the National Key Program for Developing Basic Sciences of China (No. 2006CB400506), National Natural Science Foundation of China (No. 40675007), Natural Science Foundation of Yunnan Province of China (2005D0006M), Project for innovative research team of high performance computing in Yunnan University. We thank Dr. Yongsheng Chen for his great help in revision.

### References

- Adler RF, Susskind J, Huffman GJ, Bolvin D, Nelkin E, Chang A, Ferraro R, Gruber A, Xie P-P, Janowiak J, Rudolf B, Schneider U, Curtis S, Arkin P (2003) The Version-2 Global Precipitation Climatology Project (GPCP) monthly precipitation analysis (1979-present). *J Hydrometeorol* 4(6): 1147–67
- Betts AK, Harshvardhan (1987) Thermodynamic constraint on the cloud liquid water feedback in climate models. *J Geophys Res* 92(D7): C8483–5
- Bond TC, Streets DG, Yarber KF, Nelson SM, Woo J, Klimont Z (2004) A technology-based global inventory of black and organic carbon emissions from combustion. *J Geophys Res* 109: D14203; DOI: 10.1029/2003JD003697
- Cao JJ, Lee SC, Ho KF, Zhang XY, Zou SC, Fung K, Chow JC, Watson JG (2003) Characteristics of carbonaceous aerosol in Pearl River Delta Region, China during 2001 winter period. *Atmos Environ* 37: 1451–60
- Chervin RM, Schneider SH (1976) On determining the statistical significance of climate experiment with general circulation models. *J Atmos Sci* 33: 405–12
- Chung SH, Seinfeld JH (2002) Global distribution and climate forcing of carbonaceous aerosols. *J Geophys Res* 107(D19); DOI: 10.1029/2001JD001397
- Chung SH, Seinfeld JH (2005) Climate response of direct RF of anthropogenic black carbon. *J Geophys Res* 110: D11102; DOI: 10.1029/2004JD005441
- Cooke WFC, Liousse C, Cachier H, Feichter J (1999) Construction of a  $1^\circ \times 1^\circ$  fuel emission data set for carbonaceous aerosol and implementation and radiative impact in the ECHAM4 model. *J Geophys Res* 104(D18): 22, 137–162
- d'Almeida GA, Koepke P, Shettle EP (1991) Atmospheric aerosol: global climatology and radiative characteristics. A. Deepak, Hampton, VA
- Forster P, Ramaswamy V, Artaxo P, Bernsten T, Betts R, Fahey DW, Haywood J, Lean J, Lowe DC, Myhre G, Nganga J, Prinn R, Raga G, Schulz M, Van Dorland R (2007) Changes in atmospheric constituents and in radiative forcing. In: Solomon S, Qin D, Manning M, Chen Z, Marquis M, Averyt KB, Tignor M, Miller HL (eds) *Climate change 2007: the physical science basis. Contribution of Working Group I to the Fourth Assessment Report of the Intergovernmental Panel on Climate Change*. Cambridge University Press, Cambridge, United Kingdom and New York, NY, USA
- Giorgi F, Bi X, Qian Y (2002) Direct radiative forcing and regional climatic effects of anthropogenic aerosols over East Asia: a regional coupled climate-chemist/aerosol model study. *J Geophys Res* 107(D20): 4439; DOI: 10.1029/2001JD001066
- Grell G (1993) Prognostic evaluation of assumptions used by cumulus parameterizations. *Mon Wea Rev* 121: 764–87
- Hansen J, Nazarenko L (2004) Soot climate forcing via snow and ice albedos. *Proc Natl Acad Sci* 101(2): 123–428; DOI: 10.1073/pnas.2237157100
- Hansen J, Sato M, Ruedy R (1997) RF and climate response. *J Geophys Res* 102(D6): 6831–64
- Hansen J, Sato MKI, Ruedy R, Nazarenko L, Lacis A, Schmidt GA, Russell G, Aleinov I, Bauer M, Bauer S, Bell N, Cairns B, Canuto V, Chandler M, Cheng Y, Del Genio A, Faluvegi G, Fleming E, Friend A, Hall T, Jackman C, Kelley M, Kiang N, Koch D, Lean J, Lerner J, Lo K, Menon S, Miller R, Minnis P, Novakov T, Oinas V, Perlwitz JU, Perlwitz JA, Rind D, Romanou A, Shindell D, Stone P, Sun S, Tausnev N, Thresher D, Wielicki B, Wong T, Yao M, Zhang S (2005) Efficacy of climate forcings. *J Geophys Res* 110: D18104; DOI: 10.1029/2005JD005776
- Haywood JM, Shine KP (1995) The effect of anthropogenic sulfate and soot aerosol on the clear sky planetary radiation budget. *Geophys Res Lett* 22: 603–6
- Haywood JM, Roberts DL, Slingo A, Edwards JM, Shine KP (1997) General circulation model calculations of the direct RF by anthropogenic sulfate and fossil-fuel soot aerosol. *J Clim* 10: 1562–77
- He Z, Kim YJ, Ogunjobi KO, Kim JE, Ryu SY (2004) Carbonaceous aerosol characteristics of PM<sub>2.5</sub> particles in northeastern Asia in summer 2002. *Atmos Environ* 38: 1795–800
- Holtslag AAM, de Bruijn EIF, Pan H-L (1990) A high resolution air mass transformation model for short-range weather forecasting. *Mon Wea Rev* 118: 1561–75
- Jacobson MZ (2000) A physically-based treatment of elemental carbon optics: implication for global direct forcing of aerosols. *Geophys Res Lett* 27(2): 217–20
- Jacobson MZ (2001) Strong radiative heating due to the mixing state of black carbon in atmospheric aerosols. *Nature* 409: 695–7

- Jacobson MZ (2002) Control of fossil-fuel particulate black carbon and organic matter, possibly the most effective method of slowing global warming. *J Geophys Res* 107(D19): 4410; DOI: 10.1029/2001JD001376
- Jacobson MZ (2004) Climate response of fossil fuel and biofuel soot, accounting for soot's feedback to snow and sea ice albedo and emissivity. *J Geophys Res* 109: D21201; DOI: 10.1029/2004JD004945
- Kiehl JT, Hack JJ, Bonan GB, Boville BA, Breigleb BP, Williamson D, Rasch P (1996) Description of the near community climate model (ccm3), Tech Rep NCAR/TN-420+STR. National Center for Atmospheric Research
- Kirkevåg A, Iversen T (2002) Global direct radiative forcing by process-parametrized aerosol optical properties. *J Geophys Res* 107(D20): 4433; DOI: 10.1029/2001JD000886
- Koch D (2001) Transport and direct radiative forcing of carbonaceous and sulfate aerosols in the GISS GCM. *J Geophys Res* 106(D17): 20311–32
- Liao H, Seinfeld JH (2005) Global impacts of gas-phase chemistry/aerosol interactions on direct radiative forcing by anthropogenic aerosols and ozone. *J Geophys Res* 110: D18208; DOI: 10.1029/2005JD005907
- Ma ZG, Fu CB (2001) Trend of surface humid index in the arid area of northern China. *Acta Meteorologica Sinica* 59(6): 737–46 (in Chinese)
- Ma ZG, Dan L, Hu YW (2004) The extreme dry/wet events in northern China during recent 100 years. *J Geogr Sci* 14(3): 275–81
- Menon S, Hansen J, Nazarenko L, Luo Y (2002) Climate effects of black carbon aerosols in China and India. *Science* 297: 2250–3
- Myhre G, Stordal F, Restad K, Isaksen ISA (1998) Estimation of the direct RF due to sulfate and soot aerosols. *Tellus Ser B* 50: 463–77
- Pal J, Small E, Eltahir E (2008) Simulation of regional-scale water and energy budgets: Representation of subgrid cloud and precipitation processes within RegCM. *J Geophys Res* 105(D24): 29579–94
- Qian Y, Giorgi F, Huang Y, Chameides WL, Luo C (2001) Simulation of anthropogenic sulfur over East Asia with a regional coupled chemistry-climate model. *Tellus Ser B* 53: 171–91
- Ramanathan V, Crutzen PJ, Kiehl JT, Rosenfeld D (2001a) Aerosols, climate, and the hydrological cycle. *Science* 294(5549): 2119–24
- Ramanathan V, et al. (2001b) Indian Ocean experiment: an integrated analysis of the climate forcing and effects of the great Indo-Asian haze. *J Geophys Res* 106(D22): 28, 371–98
- Ramanathan V, Chung C, Kim D, Bettge T, Buja L, Kiehl JT, Washington WM, Fu Q, Sikka DR, Wild M (2005) Atmospheric brown clouds: impacts on South Asian climate and hydrological cycle. *Proc Natl Acad Sci* 12(15): 5236–333; DOI: 10.1073/pnas.0500656102
- Reddy MS, Boucher O, Bellouin N, Schulz M, Balkanski Y, Dufresne J-L, Pham M (2005) Estimates of global multi-component aerosol optical depth and direct radiative perturbation in the Laboratoire de Météorologie Dynamique general circulation model. *J Geophys Res* 110: D10S16; DOI: 10.1029/2004JD004757
- Roberts DL, Jones A (2004) Climate sensitivity to black carbon aerosol from fossil fuel combustion. *J Geophys Res* 109: D16202; DOI: 10.1029/2004JD004676
- Slingo JM (1989) A GCM parameterization for the short-wave radiative properties of water clouds. *J Atmos Sci* 46: 1419–27
- Streets DG, Bond TC, Carmichael GR, Fernandes SD, Fu Q, He D, Klimont Z, Nelson SM, Tsai NY, Wang MQ, Woo J-H, Yarber KF (2003) An inventory of gaseous and primary aerosol emissions in Asia in the year 2000. *J Geophys Res* 108(D21): 8809; DOI: 10.1029/2002JD003093
- Takemura T, Nakajima T, Nozawa T, Aoki K (2001) Simulation of future aerosol distribution, radiative forcing, and long-range transport in East Asia. *J Meteor Soc Japan* 79(2): 1139–55
- Takemura T, Nozawa T, Emori S, Nakajima TY, Nakayama T (2005) Simulation of climate response to aerosol direct and indirect effects with aerosol transport-radiation model. *J Geophys Res* 110: D02202; DOI: 10.1029/2004JD005029
- Uno I, Carmichael GR, Street D, Satake S, Takemura T, Woo J-H, Uematsu M, Ohta S (2003) Analysis of surface black carbon distributions during ACE-Asia using a regional-scale aerosol model. *J Geophys Res* 108(D23): 8636; DOI: 10.1029/2002JD003252
- Wang C (2004) A modeling study on the climate impact of black carbon aerosols. *J Geophys Res* 109: D03106; DOI: 10.1029/2003JD004084
- Wu J, Jiang WM, Fu CB, Su BK, Liu HN, Tang JP (2004) Simulation of the radiative effect of black carbon aerosols and the regional climate responses over China. *Adv Atmos Sci* 21(4): 637–49
- Ye B, Ji X, Yang H, Yao X, Chan CK, Cadle SH, Chan T, Mulawa PA (2003) Concentration and chemical composition of PM<sub>2.5</sub> in Shanghai for a 1-year period. *Atmos Environ* 37: 499–510
- Zeng XB, Zhao M, Dickson RE (1998) Intercomparison of bulk aerodynamic algorithms for the computation of sea surface fluxes using TOGA COARE and TAO Data. *J Climate* 11(10): 2628–44
- Zhang MG, Xu YF, Zhang RJ (2005) Emission and concentration distribution of black carbon aerosol in East Asia during springtime. *Chinese J Geophys* 48(1): 46–51 (in Chinese)